

A study on the average wind load characteristics and wind-induced responses of a super-large straight-cone steel cooling tower

S.T. Ke^{*1,2}, L.Y. Du^{1a}, Y.J. Ge^{2b}, L. Zhao^{2c} and Y. Tamura^{3d}

¹Department of Civil Engineering, Nanjing University of Aeronautics and Astronautics, 29 Yudao Road, Nanjing 210016, China

²State Key Laboratory for Disaster Reduction in Civil Engineering, Tongji University, 1239 Siping Road, Shanghai 200092, China

³Center of Wind Engineering Research, Tokyo Polytechnic University, 1583 Iiyama, Atsugi, Kanagawa 243-0297, Japan

(Received February 25, 2017, Revised October 28, 2017, Accepted November 2, 2017)

Abstract. As a novel typical wind-sensitive structure, the wind load and wind-induced structural behaviors of super-large straight-cone cooling towers are in an urgent need to be addressed and studied. A super large straight-cone steel cooling tower (189 m high, the highest in Asia) that is under construction in Shanxi Power Plant in China was taken as an example, for which four finite element models corresponding to four structural types: the main drum; main drum + stiffening rings; main drum + stiffening rings + auxiliary rings (auxiliary rings are hinged with the main drum and the ground respectively); and main drum + stiffening rings + auxiliary rings (auxiliary rings are fixed onto the main drum and the ground respectively), were established to compare and analyze the dynamic properties and force transferring paths of different models. After that, CFD method was used to conduct numerical simulation of flow field and mean wind load around the cooling tower. Through field measurements and wind tunnel tests at home and abroad, the reliability of using CFD method for numerical simulation was confirmed. On the basis of this, the surface flow and trail characteristics of the tower at different heights were derived and the wind pressure distribution curves for the internal and external surfaces at different heights of the tower were studied. Finally, based on the calculation results of wind-induced responses of the four models, the effects of stiffening rings, auxiliary rings, and different connecting modes on the dynamic properties and wind-induced responses of the tower structure were derived and analyzed; meanwhile, the effect mechanism of internal suction on such kind of cooling tower was discussed. The study results could provide references to the structure selection and wind resistance design of such type of steel cooling towers.

Keywords: steel cooling tower; straight-cone type; numerical simulation; mean wind load; wind-induced response; internal pressure effect

*Corresponding author, Associate Professor, E-mail: keshitang@163.com

^a Postgraduate, E-mail: dlynuaa@163.com

^b Professor, E-mail: yaojunge@tongji.edu.cn

^c Professor, E-mail: zhaolin@tongji.edu.cn

^d Professor, E-mail: yukio@arch.t-kougei.ac.jp

1. Introduction

A large-sized cooling tower is a tall, thin-shell structure that mainly bears wind load (Stanislaw Hlawiczka *et al.* 2016). As an important cooling facility used in the industry sector, especially in thermal power plants and nuclear power plants, a cooling tower consists of the tower drum, the brace and the circular foundation, in which the tower drum with symmetrical rotation axis is the most eye-catching component. In designing such kind of cooling towers, wind load is one of control loads. The structure's wind-resistant performance has long been a traditional topic in wind engineering research field. In light of the factors including cooling efficiency, erection cost and land use planning of a power plant, etc., sizes of the cooling tower structures are becoming increasingly large, especially for a country like China, where the energy demand is much more exuberant. Over the past decade, China has witnessed in its land the construction of the highest chimney-tower integrated cooling tower (Jiangsu Xuzhou, 2010, 167 m high), the highest wet-cooling tower (Anhui Pingwei, 2014, 181 m high) and the highest high-level tower (Shandong Shouguang, 2015, 191 m high) in Asia. A super large cooling tower to be used in Jiangxi Pengze Nuclear Power Plant has been predicted to be 250m high. Fig. 1 shows the height evolution of the cooling towers at home and abroad.

As a novel cooling tower structure, steel cooling tower enjoys such advantages like fast construction speed, recyclable, and not limited by winter temperature. There are already a dozen of successful cases in the world, which are applied in indirect air cooling of power plants. In China, however, construction of steel cooling towers is still in infant stage. Only one hyperbolic cooling tower is under construction, which is a 160m-high tower in Xinjiang Power Plant. Most of the traditional large-scale cooling towers were made of reinforced concrete; the tower drums thereof are hyperbolic thin-walled structures. When calculation of load is concerned, such structures are normally simplified as plate and shell elements. Steel cooling towers, however, are mostly made of steel tubes with various sections, which form complex truss system with structural behaviors more similar to that of beam elements. Compared with traditional reinforced concrete cooling towers, steel cooling towers have less damping, lower frequency, more complex vibration modes and force transferring paths, and are more sensitive to wind load; therefore their problems in wind-induced dynamic amplification effect and structural behaviors are more prominent.

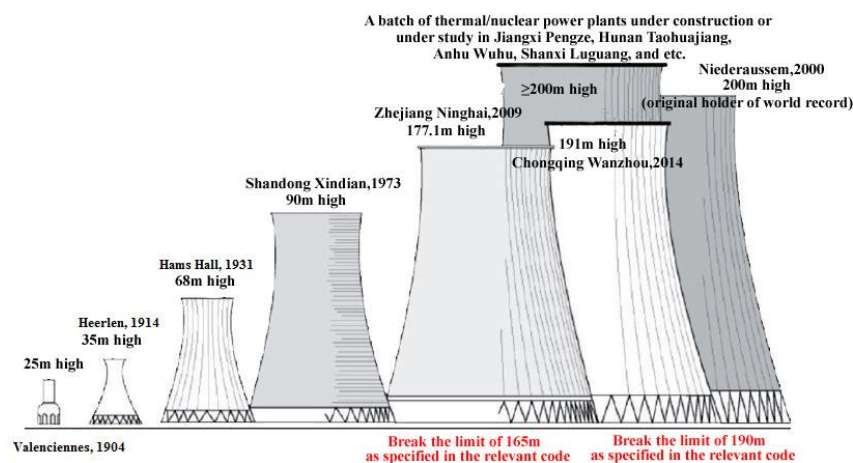


Fig. 1 Height evolution of the cooling towers at home and abroad

With regard to wind resistance of large-sized cooling towers, domestic and foreign scholars, using wind tunnel tests, numerical modeling and field measurement methods, have conducted in-depth researches on the wind load (Viladkar *et al.* 2006, Wittek and Grote 2015, Cheng *et al.* 2015), interference effect (Niemann and Kopper 1998, Zhao and Ge 2010, Ke *et al.* 2012), wind-induced response (Busch *et al.* 2002, Babu *et al.* 2013, Ke *et al.* 2013), overall and local stability (Baillis *et al.* 2000, Goodarzi 2010, Zhang *et al.* 2014) of large-sized reinforced concrete hyperbolic cooling towers. The research results obtained well guided the wind resistant design of traditional reinforced concrete cooling towers. Yet for steel cooling towers, researches on wind resistance thereof are not enough. Izadi *et al.* (2014) systemically studied dynamic response characteristics of hyperbolic steel cooling towers under the action of earthquake and wind load, on the basis of which they optimized the grid structure of hyperbolic steel cooling towers. Shimaoka *et al.* (2005) studied the structural behaviors and integral & local stability of large-sized hyperbolic steel cooling towers. However, in those literatures, wind load and wind-induced structural behaviors of large-sized straight-cone type steel cooling towers were seldom involved. The line style of straight-cone type steel cooling towers differs greatly from that of traditional hyperbolic cooling towers. As no explicit surface static wind load distribution and structural behaviors of straight-cone type steel cooling towers are given in the existing codes and literatures, engineering design and research personnel in this field are facing a lot of puzzles.

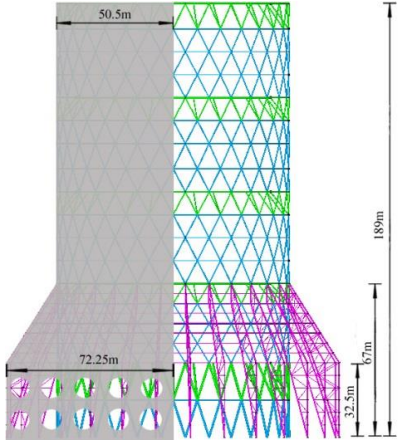
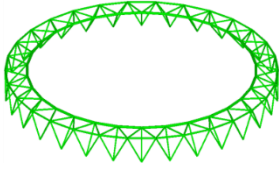
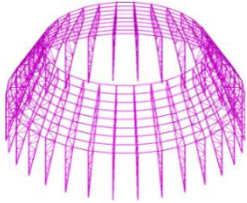
In view of this, in this paper, a super large straight-cone steel cooling tower (189 m high) that is under construction in Shanxi Power Plant in China was taken as an example, for which four finite element models corresponding to four structural types, including the main drum, main drum + stiffening rings, main drum + stiffening rings + auxiliary rings (auxiliary rings are hinged with the main drum and the ground respectively), and main drum + stiffening rings + auxiliary rings (auxiliary rings are fixed onto the main drum and the ground respectively), were established to analyze the dynamic properties and force transferring paths of different models. CFD method was used to conduct numerical simulation of flow field and mean wind load around the cooling tower, from which the surface flow and trail characteristics of the tower were derived and the wind pressure distribution curves for the internal and external surfaces for different heights of the tower were presented. Based on the calculation results of wind-induced responses, the effects of stiffening rings, auxiliary rings, connecting modes, and internal pressure on the wind-induced responses of the tower were systemically compared and analyzed. The results of which could provide references to the wind load design parameters for such type of steel cooling towers.

2. Analysis of dynamic properties

2.1 Finite element modeling

This super-large straight-cone steel cooling tower is supported from the inside by steel frames, it consists of the main drum, the stiffening trusses and the auxiliary trusses. Both the main drum (18 layers) and the stiffening rings (5 layers) are made of Q345 steel. The auxiliary trusses, 30 frames in total, are made of Q235B steel, the tower is 189 m high. Its air intake is located at a height of 32.5 m with a diameter of 144.5 m. Above the air intake, the structure is covered with wind-shielding steel plates in smooth surfaces. The main physical dimensions and the sketch of structure of cooling tower are shown in Table 1.

Table 1 Main physical dimensions and the sketch of structure of the super-large steel cooling tower

Design parameters	Value /m	Sketch of Integral Structure	Sketch of Local Structure
Tower crest level	189		
Inner diameter of air outlet	85		
Diameter of air outlet	101		
Crest level of cone section	67		Stiffening ring
Height of air intake	32.5		Auxiliary ring
Diameter of air intake	144.5		
Tower bottom level	0		
Tower bottom diameter	144.5		

For the convenience of expression, the calculation models corresponding to the four structural types, including the main drum, main drum + stiffening rings, main drum + stiffening rings + auxiliary rings (auxiliary rings are hinged with the main drum and the ground respectively), and main drum + stiffening rings + auxiliary rings (auxiliary rings are fixed onto the main drum and the ground respectively), are referred to as Models 1, 2, 3, and 4, respectively. An universal software, ANSYS, was used to establish finite element models for the four structural types, which are as shown in Fig. 2, among them, all the bars were discreted to beam188 elements. In Model 1, the diagonal members at the bottom of the tower are solidly fixed onto the ground; in Model 2, the external nodes of the stiffening rings share the corresponding nodes on the main drum; in Model 3, the upper part of the auxiliary rings is hinged with the main drum, and the lower part with the ground; in Model 4, the upper part of the auxiliary ring is fixed onto the main drum and the lower part onto the ground.

The surface skin of the steel cooling tower doesn't provide structural stiffness. But considering the fact that the mass of the skin will cause certain effect on the subsequent modal and wind-induced response analysis, the mass of the skin is allowed for by increasing the density of the ring members, i.e., the steel density in the models multiplied by a factor of 1.15 is considered as the integral equivalent density of the steel cooling tower.

2.2 Analysis of dynamic properties

Figs. 3 and 4 show vibration modes of the four models at the base-order and 50th-order, respectively. Through comparison it was found that the vibration mode of the main drum structure

without stiffening rings was complex and displayed relatively large deformation as well as obvious 3D characteristics; the number of circumferential and vertical harmonic waves increased with the order of the vibration. Provision of stiffening rings imposed obvious restriction to the circumferential and vertical deformation of the model. In addition, as the connecting cross bars between each frame of the auxiliary ring have relatively weak strength, the main deformation of Model 3 and Model 4 at base order was transferred from the main drum to the auxiliary rings, which can be seen from the circumferential twisting of the auxiliary rings. Along with increase of the order, the main deformation of Model 3 was transferred from the auxiliary rings to the tower crest.

Fig. 5 illustrates the natural vibration frequency curves of the four models from base order to the 100th order. As revealed in the figure: 1) Model 2 has the largest natural vibration frequency, which increased rapidly from base order to 20th order and slowed down thereafter; 2) Model 1 displayed a linear regular distribution of natural vibration frequency, with the value from base order to the 10th order being the smallest; 3) auxiliary trusses is connected weakly with the main drum and own big flexibility, hence, they increase the mass and reduced the rigid of whole structure, in turn, lead to decrease the natural frequencies; those of Model 3 and Model 4 were very close to each other from base order to the 10th order; Model 4's natural vibration frequency was larger than that of Model 3 within 10~35th order and smaller than that of Model 3 after the 35th order; 4) a flat frequency line was observed in Model 3 from 10th to 35th order, which was almost invariable; a longer one was observed in Model 4, from 10th to 65th order.

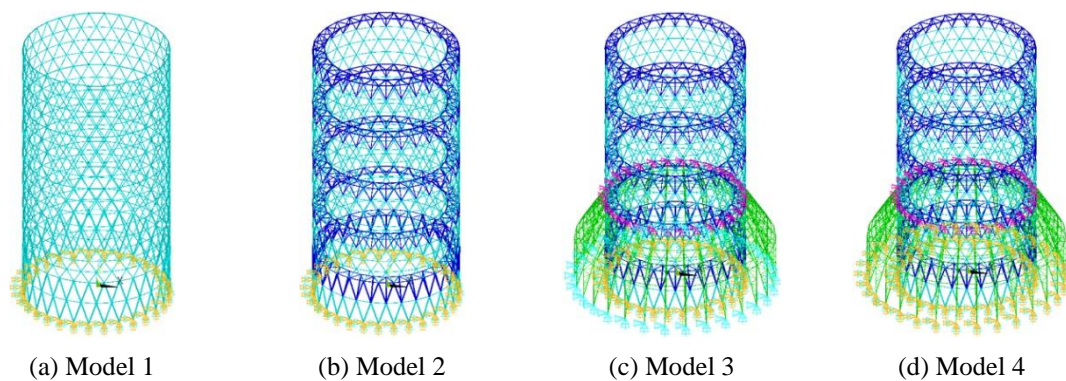


Fig. 2 Finite element models of the steel cooling tower

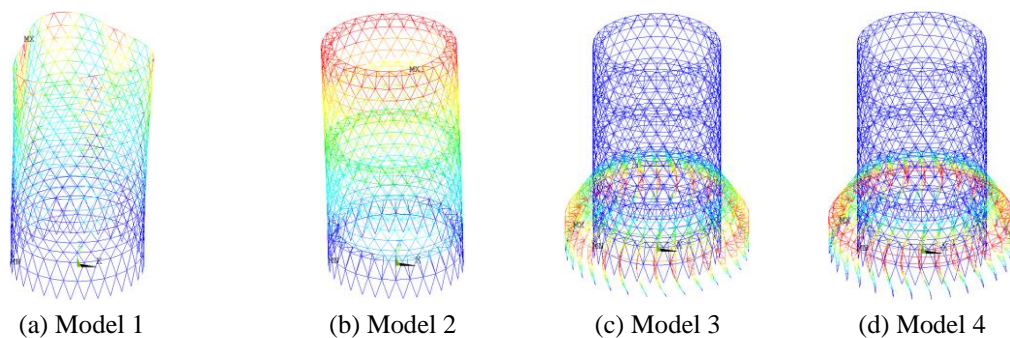


Fig. 3 Vibration modes of the four models at the base-order

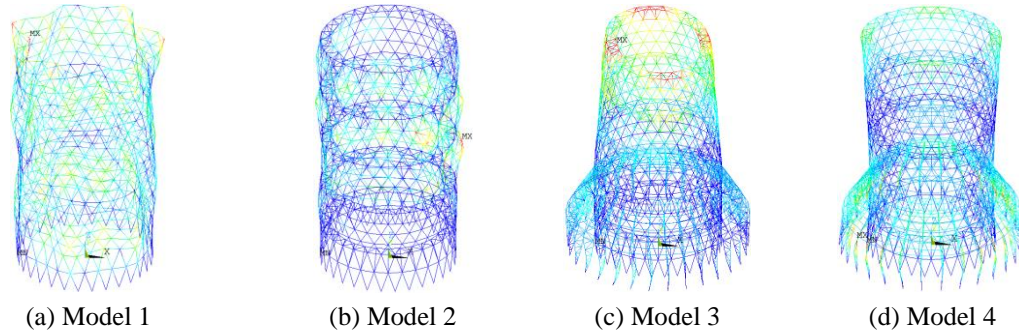


Fig. 4 Vibration modes of the four models at the 50th-order

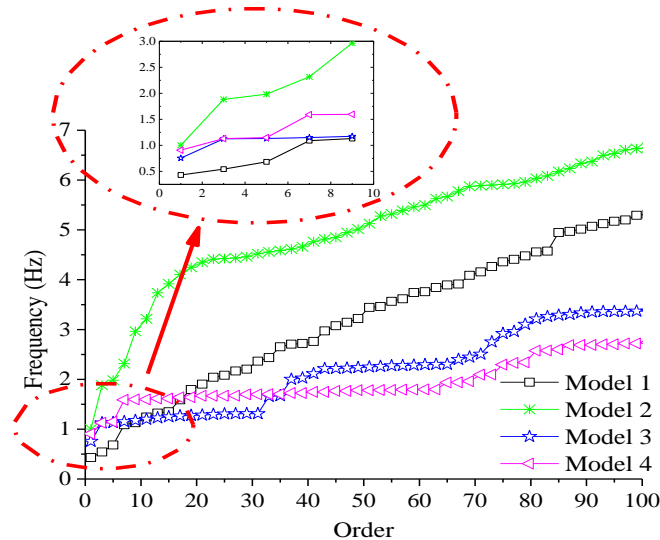


Fig. 5 Natural vibration frequency curves of the four models from base order to the 100th order

3. Numerical simulation of mean wind load

3.1 Grid division and parameters setting

Model 1 and Model 2 have typical circular sections, so the wind pressure distribution curve for circular sections as provided in the Load Code for the Design of Building Structures (GB50009-2012, 2012) was applied directly. For Model 3 and Model 4, CFD technology was applied to conduct numerical simulation of mean wind load. The three dimensional models was established with the actual sizes in Rhinoceros software and 30% ventilation rate was applied to allow for the on-state of shutters (Ke *et al.* 2015). Then export the .stl format file and join the ICEM CFD software for pre-processing, the Reynolds member of the steel cooling tower is around

$8 \times 10^7 \sim 3 \times 10^8$. To achieve both calculation efficiency and precision, the entire computational domain is divided into the periphery area and the local intensive area. The periphery area has a smooth shape and is divided by high quality structured grids. The local intensive area incorporates the cooling tower Model and is divided by unstructured grids. The number of the total grids is about 16,400,000 and the minimum size of the grids is 0.2 m, the yplus value is 47.1. Fig. 6 displays the entire computational domain and the model grid division.

The landform in which the steel cooling tower is located falls into type *B*, where the ground roughness coefficient α is 0.15. The velocity profile and turbulence level at the inlet are expressed as exponential rates. The mathematical expressions showing their changes along height direction are shown in equations 1~3. Of which, U_0 is the maximum average wind velocity with return period of 50 years when $Z_0=10$ m (height), which is taken as 26.83 m/s. Z is the distance between the calculated height and the ground; and I_{10} is nominal turbulence level at the height of 10 m, which is taken as 0.14.

$$U_z = U_0 \left(\frac{Z}{Z_0} \right)^\alpha \quad (1)$$

$$I_z(z) = I_{10} \bar{I}_z(z) \quad (2)$$

$$\bar{I}_z(z) = \left(\frac{z}{10} \right)^{-\alpha} \quad (3)$$

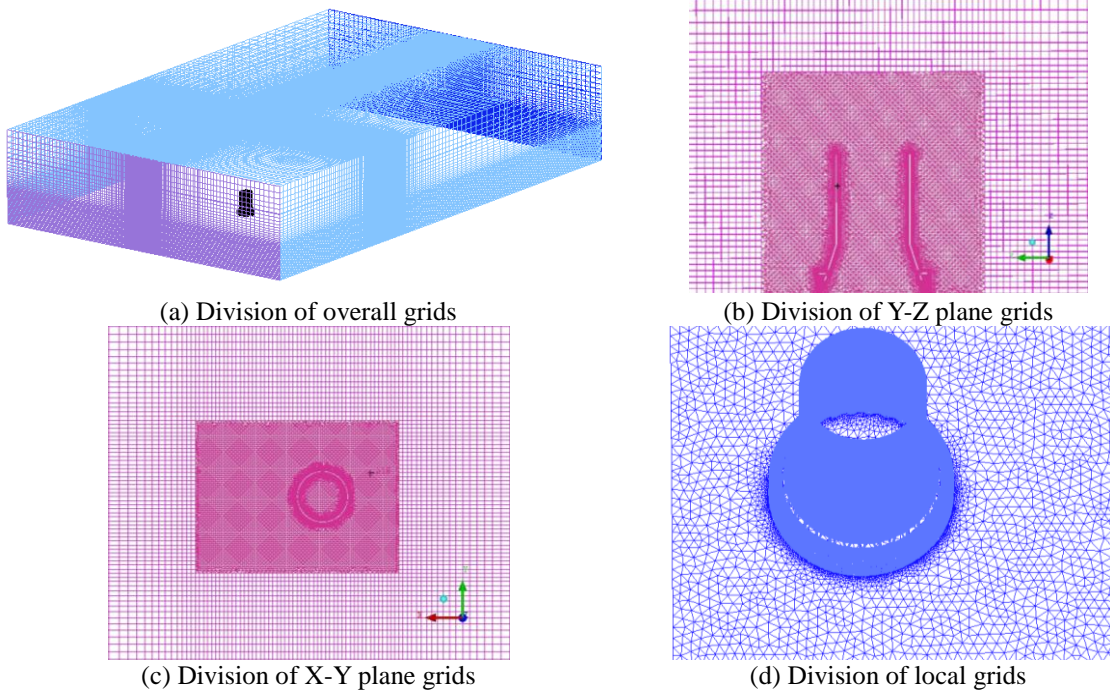


Fig. 6 Computational domain and model grid division

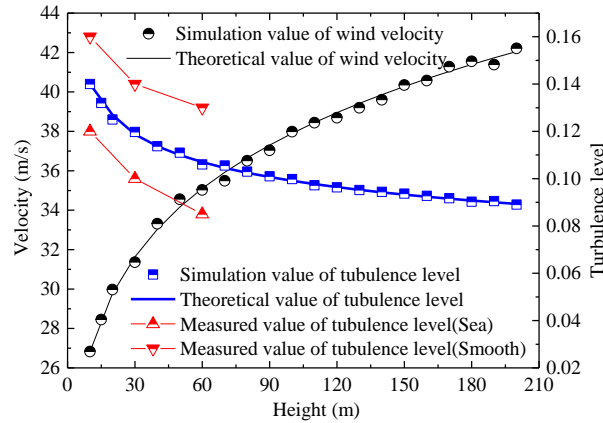


Fig. 7 Distribution of average wind profile and turbulence intensity

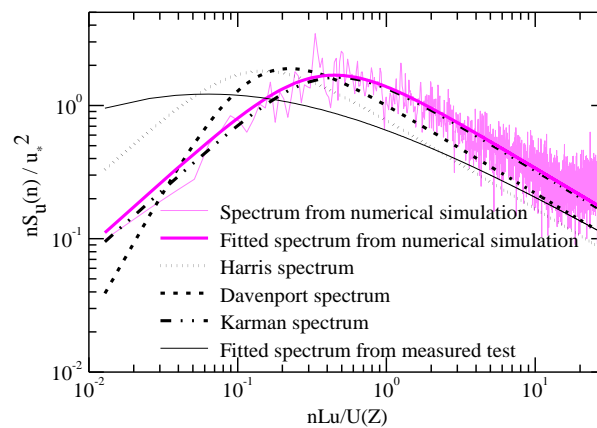


Fig. 8 Fluctuating wind spectrum generated from numerical simulation

In Fig. 7, a comparison between the simulation values, theoretical values and some measured values (Li *et al.* 2015) of average wind velocity and turbulence level profile at the atmospheric boundary layer is given. The fluctuating wind spectrum generated from numerical simulation was fitted and compared with Davenport spectrum, Harris spectrum, Karman spectrum and measured spectrum (Wang *et al.* 2016), which are as shown in Fig. 8. Comparison in the figure shows that the simulation values of wind average wind velocity and turbulence level profile are in good agreement with the theoretical values, and located between the two measured curves. The fitted wind spectrum from numerical simulation is quite coincided with the Karman spectrum, and its distribution law is similar to the other two traditional wind spectrums and the measured wind spectrum. Thus, the wind field simulation standard obtained from the numerical simulation can meet the project requirements. The parameters adopted for CFD numerical simulation in FLUENT software are shown in Table 2 (Jeong 2004).

Table 2 Calculating parameters used in numerical simulation

Parameter	Parameter setting
Solver type	3D single precision, discrete solver
Air model	Incompressible fluid
Turbulence model	SST model
Discrete scheme of convective term	Second-order upwind scheme
Flow field calculation method	SIMPLEC algorithm
Inlet boundary condition	Velocity inlet
Outlet boundary condition	Pressure outlet
Wall boundary condition	Non-slipping wall

3.2 Flow characteristics

Fig. 9 displays the vorticity distribution of the elevation and three typical sections (the cone section, the straight drum section, and the interface area between the cone section and the straight drum section); Fig. 10 displays the superimposition of the pressure cloud picture and the velocity streamline for the elevation and three typical sections. A comparison over the figures showed that:

1) In the wind shadow area, the vorticity firstly increased with the tower height and later decreased, with the peak value appeared at the middle of the tower drum. Along the wind direction, the vorticity change was contrary to that in the wind shadow area. Compared with the interface section and the straight drum section, the vorticity increase area in the wind shadow area of the cone section along the across-wind direction was relatively large and the separation point appeared earlier.

2) Along the height direction of the tower drum, the pressure and velocity in the wind shadow area firstly increased and then decreased, with the peak value appeared at the middle of the tower drum, but with relatively weak backflow and vortex. The pressure field and velocity field at both sides of the cooling tower displayed a basically symmetrical distribution around the wind axis. In the windward areas, the flow separation points of different sections were basically the same, but in the wind shadow areas, different sections display various degrees of backflow and vortex.

3.3 Average wind load characteristics of external surface

In aerodynamics, the pressure on the surface of an object is usually expressed as a dimensionless pressure coefficient C_{Pi}

$$C_{Pi} = \frac{P_i - P_\infty}{P_0 - P_\infty} \quad (4)$$

Where, the C_{Pi} is the pressure coefficient at the measuring point i , P_i is the pressure at the measuring point i , and the P_0 and P are respectively the total pressure and static pressure at the reference height. The shape factor of the corresponding measuring points can be obtained by the conversion of the pressure coefficient

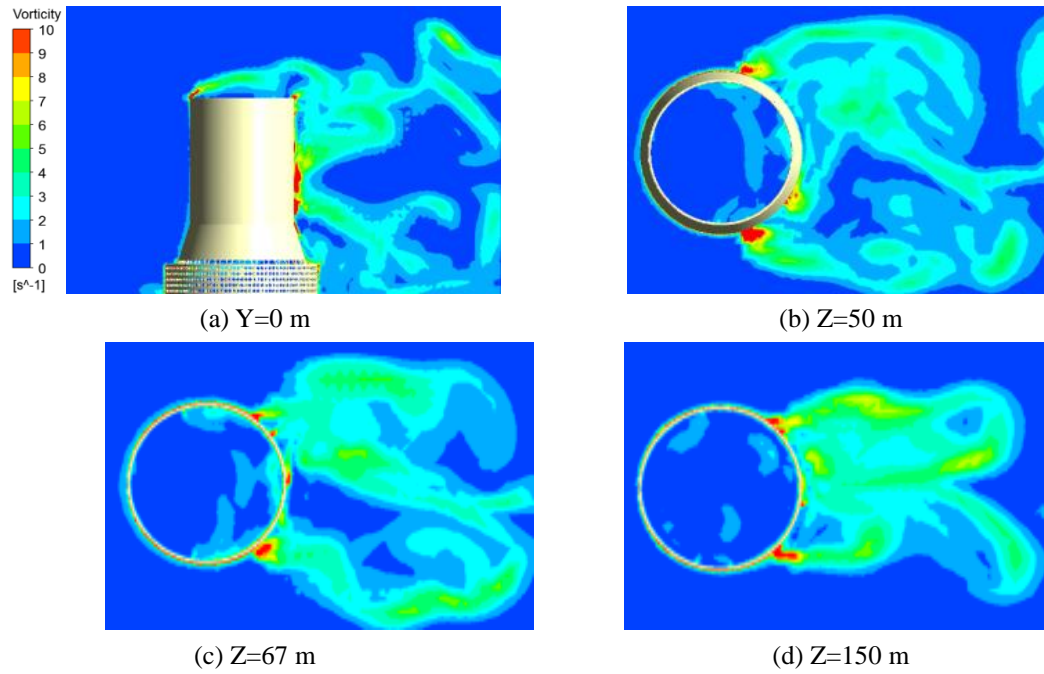


Fig. 9 Vorticity distribution of the elevation and three typical sections

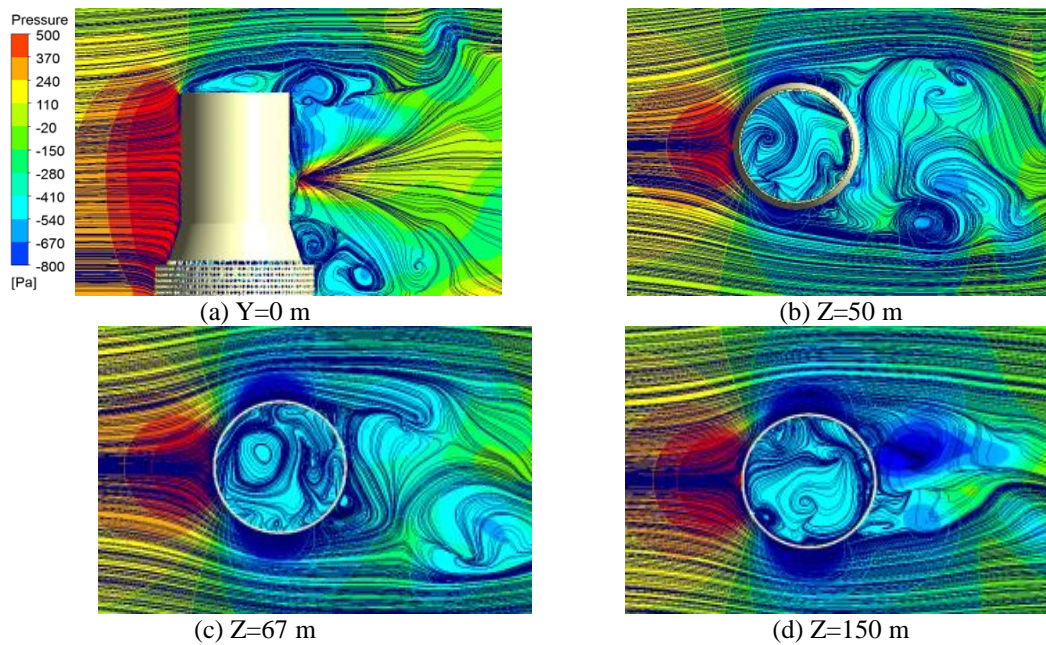


Fig. 10 The pressure cloud picture and the velocity streamline for four typical sections

$$\mu_{i,\theta} = \frac{C_{pi,\theta}}{(Z_i/h)^{2\alpha}} \quad (5)$$

Where, $\mu_{i,\theta}$ is called the shape factor at the measuring point i , Z_i is the height of the measuring point i , h is the reference point height, α is the geomorphic roughness index.

To systematically study the distribution characteristics of average wind pressure on the external surface of the super-large straight-cone steel cooling tower, the distribution curves of external surface shape factor for the cone section and the straight drum section along circumferential direction were displayed in Figs. 11 and 12, respectively.

In Fig. 11, comparison was made with the shape factor distribution curve of hyperbolic cooling towers as described in the Code for Hydraulic Design of Fossil Fuel Power Plants (DL/T 5339-2006, 2006). In Fig. 12, comparison was made with the shape factor distribution curve of circular section structures as described in the Load Code for the Design of Building Structures (GB50009-2012, 2012). An analysis of the figures indicated that: 1) for the cone section, the average shape factor of the external surface was similar to that of hyperbolic cooling towers as stated in the Code (DL/T 5339-2006, 2006); some differences were observed in the lateral wind area; at the bottom of the cone section, due to interference of air flow from the shutters and the widening platform, the surface wind pressure deviated significantly from the curve as provided in the Code (DL/T 5339-2006, 2006); 2) the shapes of straight - cone junction and the upper cylinder are different, because of the influence of the air movement and vortex shedding in this place, the average shape factor near the height of 87 m and 107 m for the straight drum is relatively larger than the media and upper area. After reaching a certain height, the interference effects gradually disappear, the average shape factor in this place is close to the code(GB50009-2012, 2012) recommended curves; due to end flow characteristics and the violent air flow, the tower crest shape factor deviated greatly from that of the circular section structures as stated in the Code (GB50009-2012, 2012); 4) the comparison results proved the reliability of using CFD method for simulating the average wind load of super-large straight-cone steel cooling towers.

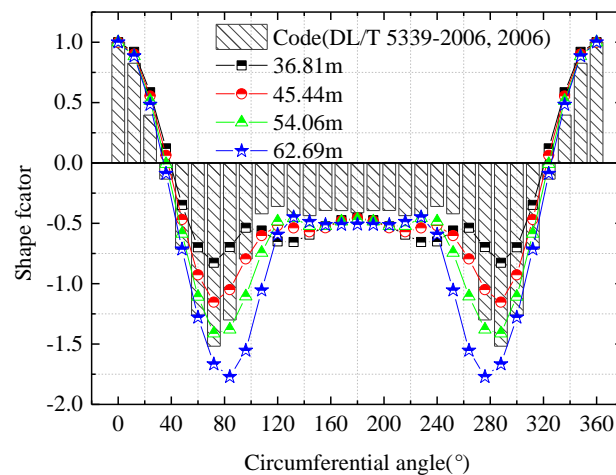


Fig. 11 Comparison of average shape factors on external surface of the cone section with the code (DL/T 5339-2006, 2006)

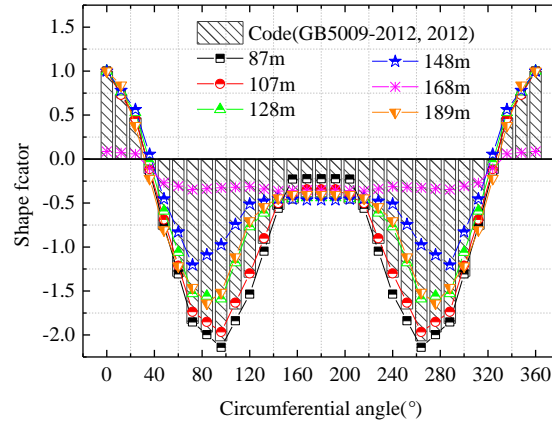


Fig. 12 Comparison of average shape factors on external surface of the straight drum section with the code (GB50009-2012, 2012)

Based on the numerical simulation results, the shape factors for the different heights of the cone section and the straight drum section were averaged and compared with that as stipulated in the relevant codes, which are displayed in Fig. 13. It was found that, for the cone section, the angles corresponding to the negative pressure extreme point and the separation point were consistent with that in the Codes (DL/T 5339-2006, 2006, VGB K1.5), but the value of negative pressure in the wind shadow area was significantly smaller than that in the code (DL/T 5339-2006, 2006); for the straight drum section, the shape factor distribution curve coincided with that of the circular section structures as stated in the Code (GB50009-2012, 2012); the shape factor in the Code (BS4485: 4-1996) is larger than that of other curves in Fig. 13, the distribution curve deviates overall. Table 3 lists the differences between the calculated shape factors and that described in relevant codes.

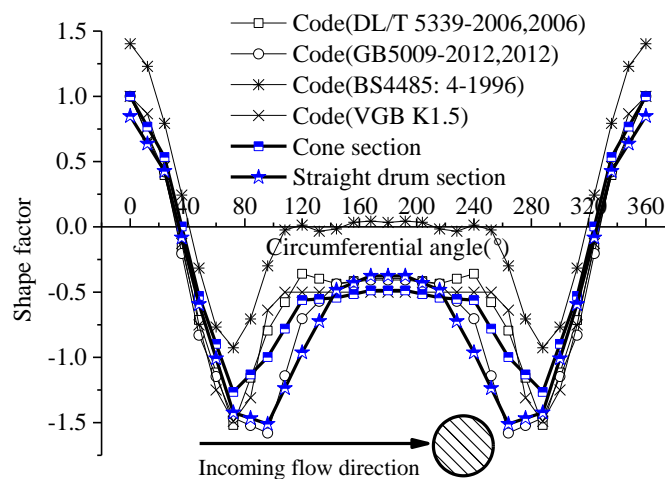


Fig. 13 Comparison between average shape factors of external surfaces

Table 3 Differences between average shape factors of external surface derived from numerical simulation and relevant codes

Circumferential angle	Cone section	Straight drum section	Circumferential angle	Cone section	Straight drum section
0°	0.0027	0.1517	180°	0.0924	0.0316
12°	0.0677	0.0728	192°	0.0924	0.0314
24°	0.1382	0.0061	204°	0.0998	0.0074
36°	0.1612	0.1216	216°	0.1071	0.0462
48°	0.1843	0.2370	228°	0.1544	0.1525
60°	0.2189	0.1392	240°	0.2017	0.2587
72°	0.2535	0.0414	252°	0.2020	0.0944
84°	0.0258	0.0556	264°	0.2023	0.0698
96°	0.2019	0.0698	276°	0.0256	0.0556
108°	0.2018	0.0944	288°	0.2535	0.0414
120°	0.2017	0.2587	300°	0.2191	0.1392
132°	0.1544	0.1525	312°	0.1848	0.2370
144°	0.1071	0.0462	324°	0.1617	0.1216
156°	0.0998	0.0072	336°	0.1386	0.0061
168°	0.0924	0.0318	348°	0.0679	0.0728

3.4 Average wind load characteristics of internal surface

Fig. 14 presents the pressure factor cloud pictures of the windward area and wind shadow area of the internal surface of the tower drum. Fig. 15(a) presents the distribution curve of internal surface shape factor of typical sections of the tower drum along circumferential direction. The shape factors of typical sections of the cone section and the straight drum section were averaged respectively to be used as input loads for subsequent internal pressure effect analysis, which are shown in Fig. 15(b). The average distribution curve of internal surface shape factors along the height direction is also shown in 15(b). A comparison over these results indicated that:

1) As the cone section is nearer to the shutters, the air flow enters into the inside of the cooling tower via the shutters. Under the action of the incoming wind pressure, the internal surface shape factor of the wind shadow area of the cone section reduced dramatically and reached its minimum value (-0.30) at 240°.

2) With the increase of the height, the shape factor of the wind shadow area of the cone section gradually approaches the value as specified in the Code (DL/T 5339-2006, 2006). However, at the interface of the cone section and the straight drum section, due to sudden reduction of windage area, the air was squeezed, causing obvious internal pressure boost. Therefore at the section with a height of 67 m, within the circumferential angle range of 90°~270°, the shape factor was obviously larger than that as specified in the Code (DL/T 5339-2006, 2006), with the maximum difference reaching 24.23%.

3) For the straight drum section, the distribution curve of the internal surface shape factor coincided with that as specified in the code for the hyperbolic cooling towers in general, with slight fluctuation and a maximum deviation of 7.12%. Along the meridian direction, the distribution was relatively uniform; along the circumferential direction, the distribution was basically symmetrical around the wind axis.

4) The distribution of internal surface shape factor of the straight drum section along circumferential direction was relatively stable, with a fluctuation of -0.49~-0.51. The average internal surface shape factor of the cone section within the range of -80°~80° coincided well with that as specified in the Code (GB50009-2012, 2012); deviation was observed in the wind shadow area, up to 18.95% at most.

4. Analysis of wind-induced responses

4.1 Selection of calculating parameters

The calculation formula of equivalent static wind load is shown in equation (6), w_k is standard value of equivalent static wind load(kN/m²); β is wind induced vibration coefficient, taken as 1.9 which is the recommended values of B type landform in the code(GB50009-2012, 2012); μ_s is wind load shape factor, for Model 1 and Model 2, the shape factors as adopted in the Load Code (GB50009-2012, 2012) for circular section structures were adopted, for Model 3 and Model 4, the external surface shape factors obtained from CFD numerical simulation were adopted; μ_z is variation factor of wind pressure height; w_0 is basic wind pressure(kN/m²), taken as 0.45KPa; C_g is the group tower amplification coefficient and taken as 1.1 (Ke *et al.* 2015) considering the effect from phase II cooling towers. The effect of internal pressure was not considered in the calculation of wind-induced responses (Du and Ke 2017).

$$w_k = \beta \mu_s \mu_z w_0 C_g \quad (6)$$

The equivalent static wind load is applied to the finite element model (as shown in Fig. 2) to calculate the wind induced responses in ANSYS. Based on the calculation results, the radial displacements of all the external nodes on the main drum, the stiffening rings and the auxiliary rings as well as the internal force response of members were derived to systematically study the effect of stiffening rings, auxiliary rings and different connecting modes on the wind-induced responses of the straight-cone steel cooling tower.

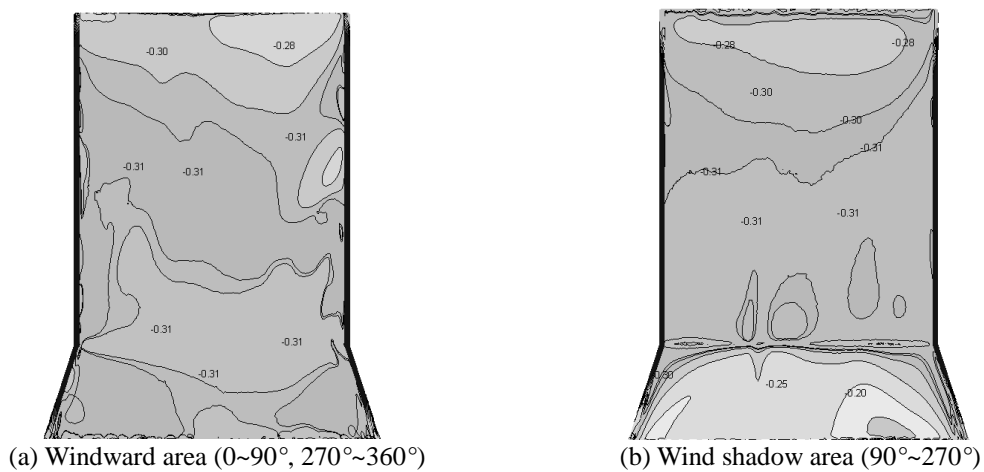


Fig. 14 Pressure factor cloud pictures of the internal surface of the steel cooling tower

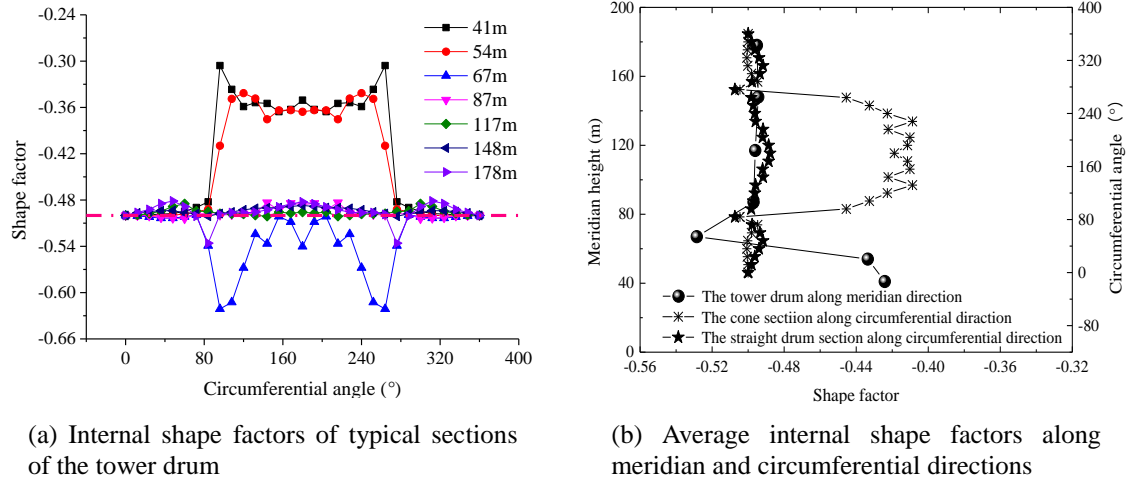


Fig. 15 Internal surface shape factor curves of the steel cooling tower

4.2 Wind-induced response of the main drum

Fig. 16 presents the radial displacement distribution of the main drum of the four models along circumferential and meridian directions. X-axis represents the circumferential angle of the cooling tower, while Y-axis represents the height of the cooling tower along the meridian direction. The color bars represent the values of displacement response. Table 4 lists the maximum and minimum values of radial displacements of the main drum in four models as well as the occurring positions. The following conclusions were drawn through comparison and analysis:

1) The radial displacements of the main drum in all the four models were symmetrical around the windward angle of 0° . The maximum negative displacement occurred around 0° , and the maximum positive displacement occurred within the range of $\pm 70^\circ \sim 100^\circ$.

2) The most significant displacement of the main drum was observed in Model 1, in which the extreme response of 33.59 cm occurred at the windward angle at the tower crest. In Model 2, the displacement of the main drum reduced dramatically, in which the extreme response of 4.44 cm occurred at the lateral wind side at a height of 49.5 m. Model 3 and Model 4 displayed a similar distribution of radial displacements, with the extreme values at the second layer of the stiffening rings. The overall radial displacement of Model 4 was smaller than that of Model 3. The provision of auxiliary rings significantly reduced the radial displacements in most part of the main drum.

Fig. 17 illustrates the axial force and torque of cross members in the windward area and negative pressure extreme area along the meridian line, while Fig. 18 displays that of the diagonal members. The following conclusions were drawn through comparison and analysis:

1) Except for Model 1, the internal force of main drum beam elements along the height direction in Models 2, 3, and 4 exhibited similar distributions.

2) Installation of stiffening rings increased the axial force of cross members in the main drum where the stiffening rings are installed, and at the same time weakened the torque of cross members and axial force of diagonal members, but had a weak effect on the torque of diagonal members of the main drum.

3) At the interface of the straight drum section and the cone section, Model 3 and Model 4 exhibited a more drastic fluctuation of internal force than that in other sections. In Model 1 and Model 2, a relatively large axial force was observed at the lower part of the main drum; the torque firstly increased with the height and then decreased, and increased again at the tower crest.

Table 4 Extreme values of radial displacements of the main drum in four models

Radial displacements	Model SN			
	Model 1	Model 2	Model 3	Model 4
Maximum positive value (cm)	29.49	4.44	4.34	3.53
Occurring position (height/angle)	189 m/-60°	49.5 m/-84°	67 m/84°	67 m/-60°
Maximum negative value (cm)	-33.59	-3.14	-6.18	-4.99
Occurring position (height/angle)	189 m /0°	49.5 m/-12°	67 m/0°	67 m /0°

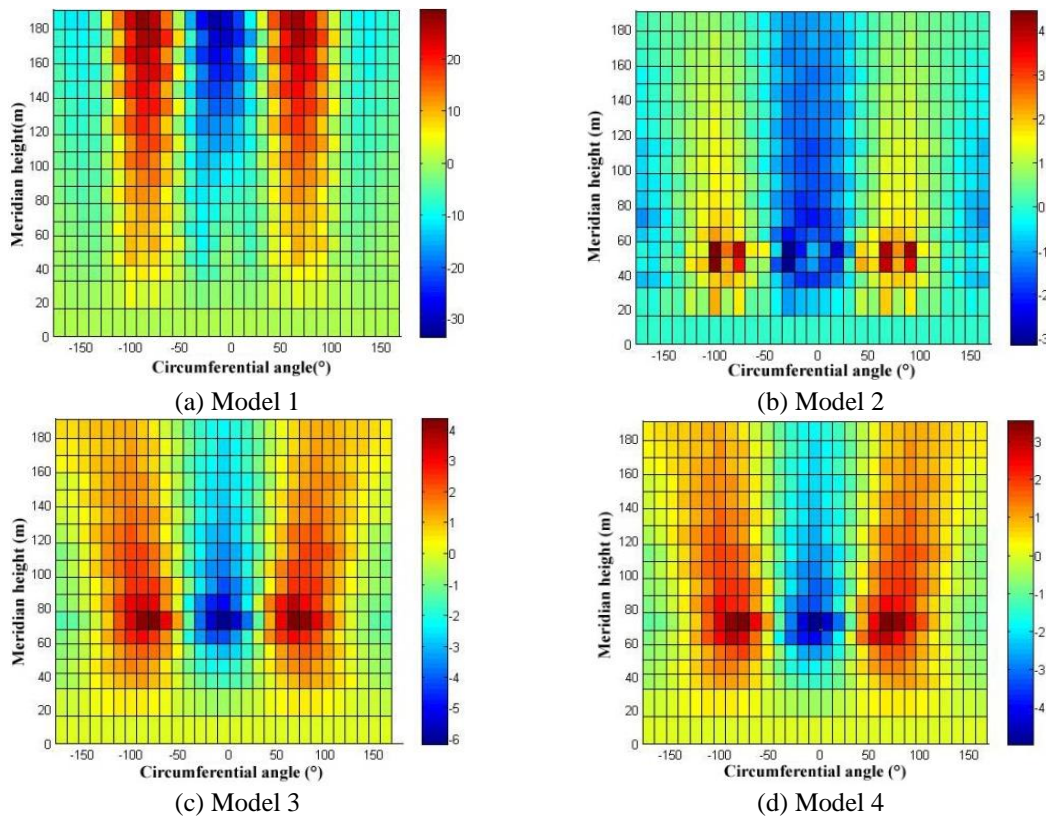


Fig. 16 Radial displacement distribution of the main drum in four models along circumferential and meridian directions

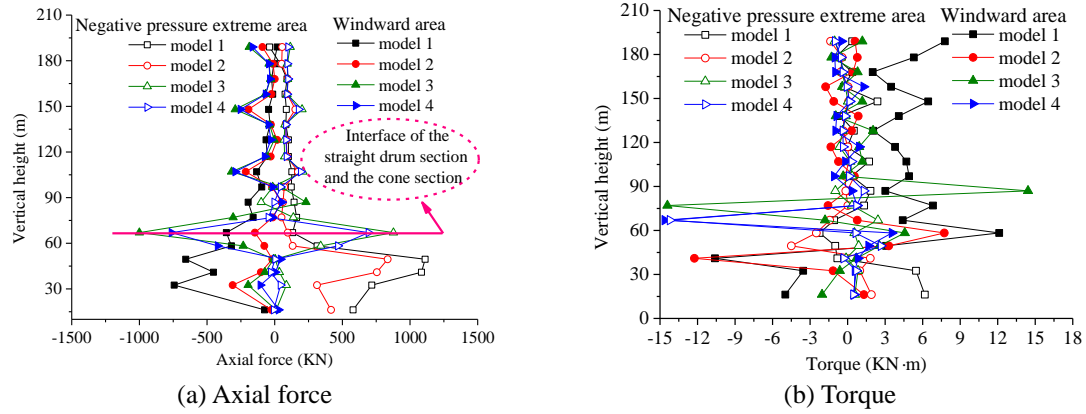


Fig. 17 Internal force response of cross members in the windward and negative pressure extreme area of main drum

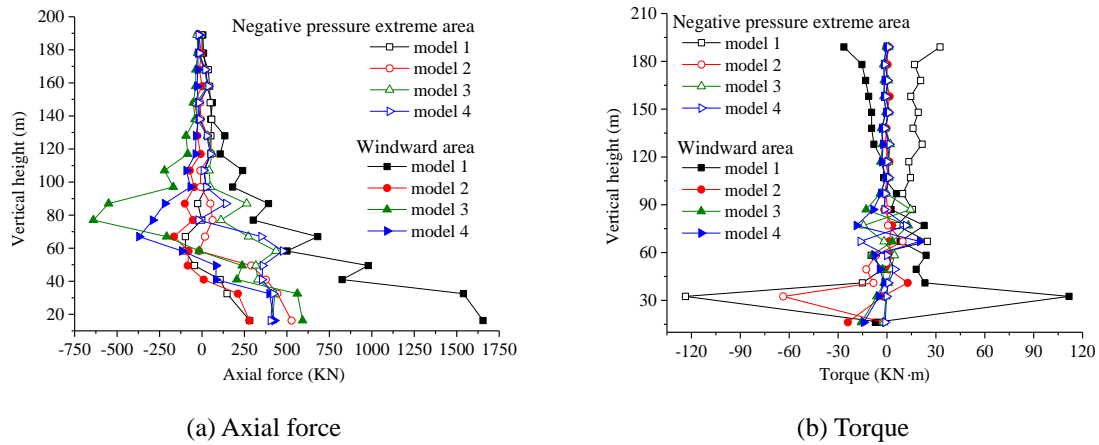


Fig. 18 Internal force response of diagonal members in the windward and negative pressure extreme area of main drum

4.3 Wind-induced response of the stiffening rings

Fig. 19 presents the radial displacement variation curves of the stiffening rings in different models. The curves for layer 1, layer 3 and layer 5 are shown respectively. Table 5 lists the extreme values and the occurring positions thereof. Analysis indicated that 1) in layer 1, Model 2 exhibited a similar distribution of radial displacement to that of Model 3 and 4 in the windward area and wind shadow area, but a varied distribution in the lateral wind area; and along with increase of height, differences in the three models became more and more obvious; 2) in layer 3 and layer 5, the largest radial displacement of stiffening rings was observed in Model 3, following by Model 4 and then Model 2; the end effect at the top layer made the displacement in the wind

shadow area of the stiffening ring in layer 5 change from negative to positive; 3) the extreme values of all the three models appeared at layer 2, in the windward area and lateral wind area of the stiffening ring; Model 2's extreme value was the smallest among the three models; Model 4 exhibited a better response than that of Model 3.

Comparison of internal force response of the stiffening rings of the three models found that the web members are mainly controlled by the axial force, while the supporting members by the torque. Fig. 20 displays the distribution of axial force of web members in the three models along the circumferential direction, and Fig. 21 displays the distribution of torque of supporting members in the three models along the same direction. Analysis indicated that:

1) The axial force distribution curves of the web members along the circumferential direction are in spiral shape and are symmetrical around the zero-axis. The maximum values of all the three models appeared at the 3rd layer stiffening ring.

2) In all the three models, the maximum torques of supporting members of stiffening rings appeared at layer 1. The curves of Model 3 and Model 4 were very smooth along the circumferential direction and displayed a trend of sine function distribution. At layer 3 and layer 5, the torques of supporting members of all the three models reduced significantly compared with that of layer 1.

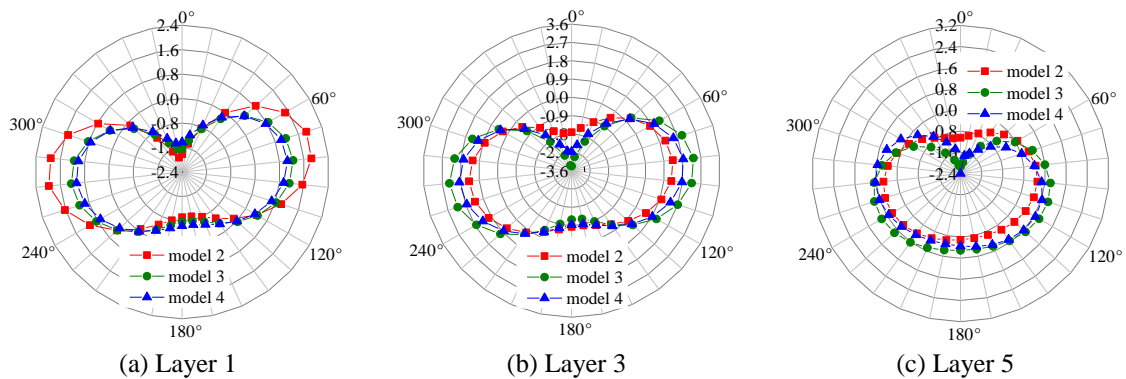


Fig. 19 Radial displacements of stiffening rings in models 2~4 along circumferential and meridian directions

Table 5 Extreme values of radial displacements of stiffening rings in models 2~4

Radial displacement(cm)	Model SN		
	Model 2	Model 3	Model 4
Maximum positive value	1.98	4.38	3.54
Maximum negative value	-2.08	-5.98	-4.82
Occurring position	290°/0° of layer 2	70°/0° of layer 2	290°/0° of layer 2

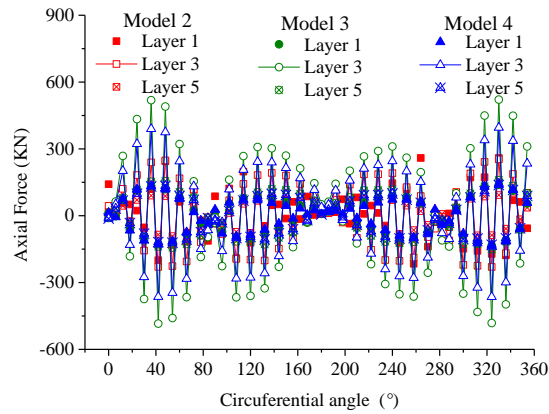


Fig. 20 Axial force distributions of the web members of the stiffening rings along circumferential direction

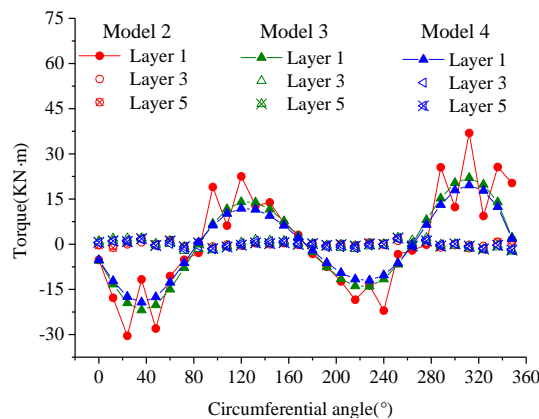


Fig. 21 Torque distributions of the supporting members of the stiffening rings along circumferential direction

4.4 Wind-induced response of the auxiliary rings

Fig. 22 illustrates the deformation and radial displacement of the auxiliary rings in Model 3 and Model 4. It was found that the two models displayed an almost identical deformation, but the radial displacement of auxiliary rings in Model 3 was slightly larger than that in Model 4.

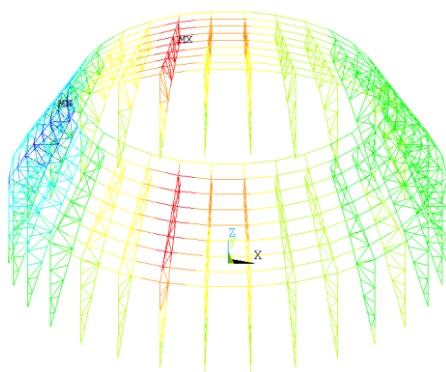
Two frames of auxiliary rings in the front windward area and negative pressure extreme value area were selected to analyze structural behaviors of the members of auxiliary rings. Fig. 23 illustrates respectively the axial force and torque distribution curves of the web members, the cross members, the internal diagonal members and the external diagonal members of the auxiliary rings of Model 3 and Model 4. The members were numbered from bottom up along vertical direction of the auxiliary rings. An analysis of the figures indicated that:

1) For the web members, the torque in the windward area was very small and almost didn't vary, except for a little deviation in the position where the auxiliary ring is connected with the

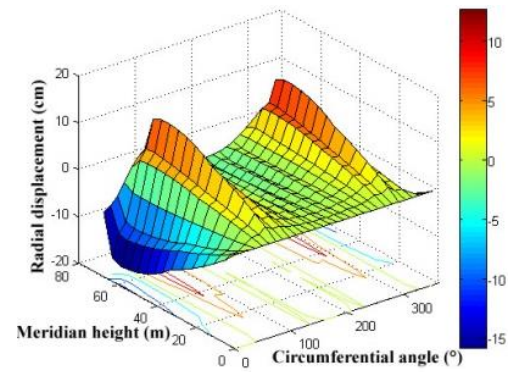
main drum. The torque in the negative pressure extreme value area was relatively large and exhibited obvious fluctuation along the height direction. The axial force of the web members displayed a trend contrary to that of the torque.

2) For the cross members, the internal force distribution of the first 7 layers of cross members was independent of the connecting mode, with a relatively stable distribution along the circumferential direction. However, due to different connecting modes between the top nodes and the main drum, the torque of the cross members at top layers of the two models developed toward contrary directions. From layer 7 upward, the axial force of the cross members in the windward area and the negative pressure extreme value area increased and decreased dramatically, respectively.

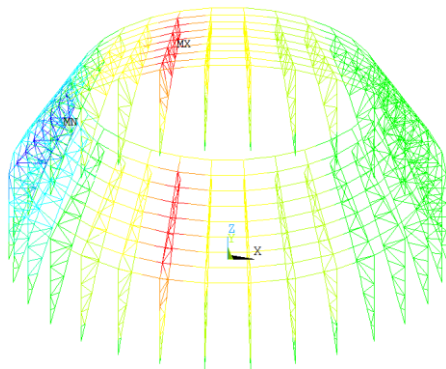
3) For the internal diagonal members, the torque in the windward area was very small and basically didn't vary along the vertical height. The torque in the negative pressure extreme value area firstly increased, and then decreased, and then increased and decreased again. The axial force in the windward area was larger than that in the negative pressure extreme value area, and exhibited a larger variation along the height direction.



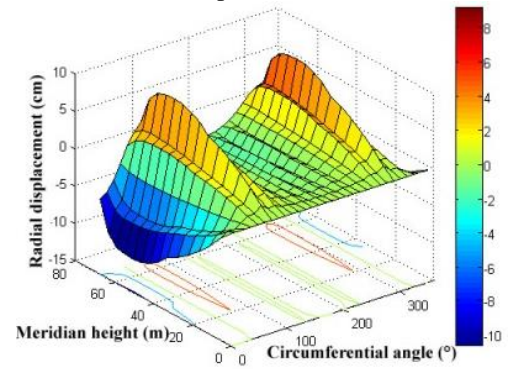
(a) Deformation of Model 3



(b) Radial displacement of Model 3



(c) Deformation of Model 4



(d) Radial displacement of Model 4

Fig. 22 Deformation and radial displacement of the auxiliary rings in Model 3 and Model 4

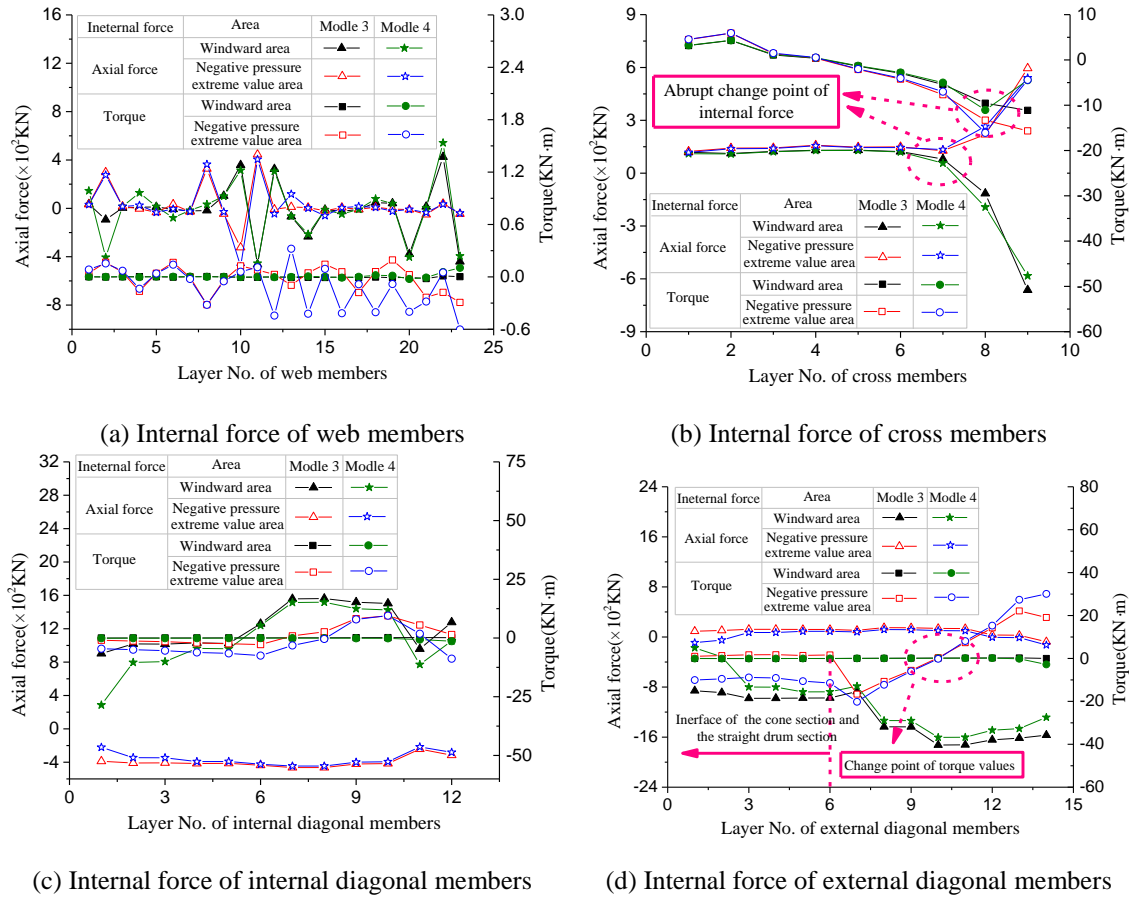


Fig. 23 Internal force responses of various members of auxiliary rings in the windward area and negative pressure extreme value area of Model 3 and 4

4) For the external diagonal members, the axial forces in the windward area and the negative pressure extreme value area developed toward contrary directions, with the axial forces in the negative pressure extreme value area larger than that in the windward area. The torque in the windward area was basically zero but deviated in the position where the auxiliary ring is connected with the main drum. The torque in the negative pressure extreme value area was stable from layer 1 to layer 6, and then increased suddenly at the interface of the cone section and the drum section of the auxiliary rings, reaching maximum negative values of $-16.64 \text{ kN}\cdot\text{m}$ (Model 3) and $-20.19 \text{ kN}\cdot\text{m}$ (Model 4), respectively; it then decreased gradually, reaching maximum positive values of $19.09 \text{ kN}\cdot\text{m}$ (Model 3) and $30.09 \text{ kN}\cdot\text{m}$ (Model 4) at the top layer.

5. Analysis of internal pressure effect

To study the effect of internal suction on the wind-induced structural behavior of the straight-cone steel cooling tower, Model 3 was taken as an example and the shape factors for the

straight drum section and the cone section derived from numerical simulation were weighted to compare the wind-induced response of each component of the cooling tower under two scenarios – with internal suction (scenario A) and without internal suction (scenario B).

Fig. 24 shows the radial displacement curves of the nodes at four heights under the two scenarios. The four heights correspond to the bottom of the cone section, the interface of the cone section and the straight drum section, the middle of the straight drum section, and the tower crest, respectively. The following conclusions were drawn after comparison and analysis:

1) The extreme values of radial displacements of the four sections under the two scenarios all occur at the front windward area and the negative pressure extreme value point.

2) Under scenario A (with internal suction), the radial displacements of the nodes at the bottom of the cone section were larger than that of other sections, with the maximum value reaching 11 cm, which occurred at the windward angle. As the tower crest is securely connected with the stiffening rings, its radial displacements were the smallest, with a maximum value of only -1.99 cm.

3) The internal suction has a weak effect on the radial displacements of the nodes on the main drum, but increased the radial displacements of the nodes in windward area of the cone section and decreased that in the lateral wind area and wind shadow area of the cone section.

Table 6 compares the wind-induced responses of the straight-cone steel cooling tower under two scenarios. It can be derived that: 1) the maximum wind-induced responses of the cooling tower under both scenarios occurred in the diagonal members of auxiliary rings in the cone section and were distributed in the positive pressure and negative pressure extreme value areas; 2) under scenario A (with internal suction), the maximum general displacement, maximum pressure, and maximum positive bending moment increased, while the maximum tension and maximum negative bending moment decreased; 3) under the reference wind velocity, the internal suction imposed a maximum effect of 12.12% on the extreme value of the axial compressive force and a minimum effect of 2.20% on the extreme value of the axial tensile force.

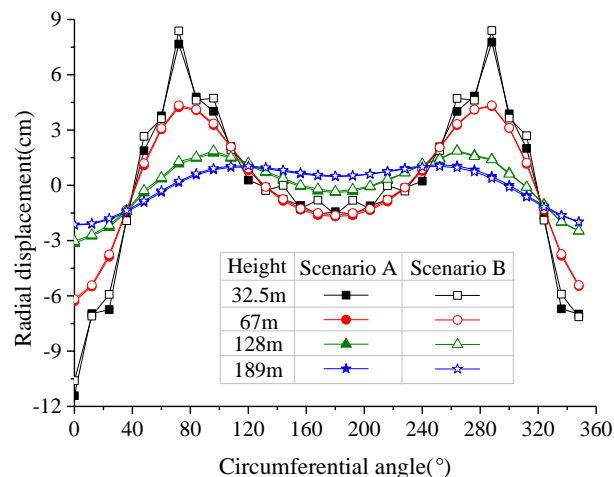


Fig. 24 Radial displacement curves of the nodes at four heights under two scenarios

Table 6 Comparison of wind-induced responses of the steel cooling tower under two scenarios

Scenario	Maximum general displacement (cm)	Maximum axial force (kN)		Maximum bending moment (kN·m)	
		Positive value	Negative value	Positive value	Negative value
With internal suction	17.96	2220	-2220	770.96	-519.19
Without internal suction	16.67	2270	-1980	693.92	-570.21
Changed percentage	7.74%	-2.20%	12.12%	11.10%	-8.95%
Occurring position	Diagonal members of auxiliary rings in the cone section				
Occurring area	Front windward area	Negative pressure extreme value area	Front windward area	Front windward area	Negative pressure extreme value area

6 Conclusions

The wind pressure distribution of the internal and external surfaces and the wind-induced response characteristics of the steel cooling tower were systematically studied, in which the CFD numerical simulation, finite element modeling, dynamic property analysis, wind-induced response calculation, and internal pressure effect discussion, etc. were involved. The following conclusions were drawn:

- For the straight drum section, the average shape factor of external surface was very similar to that of circular section structures as provided in the Code (GB50009-2012, 2012) in the windward area and wind shadow area; significant difference was observed in the lateral wind area; the internal surface shape factor coincided with that as specified in the Code. For the cone section, the average shape factor of the external surface was similar to that of hyperbolic cooling towers as stated in the Code (DL/T 5339-2006, 2006, VGB K1.5); but due to interference of air flow from the shutters and the widening platform, the surface wind pressure deviated significantly from the curve as provided in the Code, and the average shape factor of internal surface of the wind shadow area reduced sharply, that of the windward area, however, coincided well with that as specified in the Code.
- The most significant displacement of the main drum was observed in Model 1, in which the extreme response occurred at the tower crest. Installation of stiffening rings significantly reduced the displacement of the main drum in Model 2, with the extreme value shifted downward to the middle-lower part of the tower. Provision of auxiliary rings significantly reduced the displacement of the main drum in Model 3 and Model 4, in which the maximum radial displacements were transferred to the auxiliary rings, the overall radial displacement of Model 4 was smaller than that of Model 3.
- Installation of stiffening rings increased the axial force of cross members of the main drum where the stiffening rings are installed, and weakened the torque of cross members and axial force of diagonal members, but had a weak effect on the torque of diagonal members of the main drum; installation of auxiliary rings lead to a more drastic fluctuation of internal force at the interface of the straight drum section and the cone section than that in other sections, and made the torque of supporting members in the stiffening rings display a sine function distribution along circumferential direction. The connecting mode of the auxiliary rings with the main drum has a

relatively large effect on the torque values of cross members locating on the top layers of the auxiliary rings.

- The internal suction has a weak effect on the radial displacements of the nodes on the main drum, but increased the radial displacements of the nodes in the windward area of the cone section and decreased that in the lateral wind area and wind shadow area of the cone section. The internal suction has a relatively significant effect on the response extreme values of the entire structure, which has a maximum effect of 12.12% on the extreme value of the axial compressive force.

Acknowledgments

This project is jointly supported by National Natural Science Foundation (51208254; U1733129 and 5171101042), Jiangsu Province Natural Science Foundation (BK2012390), and Postdoctoral Science Foundation (2013M530255 and 1202006B), Jiangsu Universities Qing Lan Project and Six Talent Peaks Project in Jiangsu Province (JZ-026) which are gratefully acknowledged.

References

- Babu, G.R., Rajan, S.S., Harikrishna, P., Lakshmanan, N. and Arunachalam, S. (2013), "Experimental determination of wind-Induced response on a model of natural draught cooling tower", *Exp. Techniques*, **37**(1), 35-46.
- Baillis, C., Jullien, J.F. and Limam, A. (2000), "An enriched 2D modelling of cooling towers.: Effects of real damage on the stability under self-weight and on the strength under wind pressure", *Eng. Struct.*, **22**(7), 831-846.
- BS4485 (Part 4) (1996), "Code of practice for structural design and construction-water cooling tower", *London: British Standard Institution*.
- Busch, D., Harte, R., Kratzig, W.B. and Montag, U. (2002), "New natural draught cooling tower of 200 mheight", *Eng. Struct.*, **24**(12), 1509-21.
- Cheng, X.X., Zhao, L., Ge, Y.J., Ke S.T. and Liu X.P. (2015), "Wind pressures on a large cooling tower", *Adv. Struct. Eng.*, **18**(2), 201-220.
- DL/T 5339-2006 (2006), "Code for hydraulic design of fossil fuel power plants", *The Ministry of Construction of China, Beijing: China*, 115-116. (in Chinese)
- Du, L.Y. and Ke, S.T. (2017), "Research on effect of internal pressures for super large cylinder-conic section steel cooling towers", *The Journal of Central South University*, accepted but not published. (in Chinese)
- GB50009-2012 (2012), "Load code for the design of building structures", *The Ministry of Construction of China, Beijing, China*, 35-36. (in Chinese)
- Goodarzi, M. (2010), "A proposed stack configuration for dry cooling tower to improve cooling efficiency under cross wind", *J. Wind Eng. Ind. Aerod.*, **98**(12), 858-863.
- Izadi, M. and Bargi, K. (2014), "Natural draft steel hyperbolic cooling towers: Optimization and performance evaluation", *Struct. Des. Tall Spec. Build.*, **23**, 713-720.
- Jeong, S.H. (2004), "Simulation of large wind pressures by gusts on a bluff structure", *Wind Struct.*, **7**(5), 333-344.
- Ke, S.T., Ge, Y.J. and Zhao, L. (2015), "Wind-induced vibration characteristics and parametric analysis of large hyperbolic cooling towers with different feature sizes", *Struct. Eng. Mech.*, **4**(5), 891-908.
- Ke, S.T., Ge, Y.J., Zhao, L. and Tamura Y. (2012), "A new methodology for analysis of equivalent static wind loads on super-large cooling towers", *J. Wind Eng. Ind. Aerod.*, **111**(3), 30-39.

- Ke, S.T., Ge, Y.J., Zhao, L. and Tamura, Y. (2013), "Wind-induced Responses Characteristics on Super-large Cooling Towers", *J. Central South Univ. Technol.*, **20**(11), 3216-3227.
- Ke, S.T., Liang, J., Zhao, L. and Ge, Y.J. (2015), "Influence of ventilation rate on the aerodynamic interference for two IDCTs by CFD", *Wind Struct.*, **20**(3), 449-468.
- Li, L.X., Kareem, A., Xiao, Y.Q. and Zhou, C. (2015), "A comparative study of field measurements of the turbulence characteristics of typhoon and hurricane winds", *J. Wind Eng. Ind. Aerod.*, **140**, 49-66.
- Niemann, H.J. and Kopper, H.D. (1998), "Influence of adjacent buildings on wind effects on cooling towers", *Eng. Struct.*, **20**(10), 874-880.
- Shimaoka, S., Nakazawa, S., Kato, S., Shibata, R. and Okada, H. (2005), "A study on optimal parameters for buckling restrained members of steel cooling tower: Application of grid computing system", *Summaries of technical papers of Annual Meeting Architectural Institute of Japan. B-1, Structures I, Loads, reliability stress analyses foundation structures shell structures, space frames and membrane structures. Architectural Institute of Japan*, 847-848.
- Stanislaw, H., Katarzyna, K. and Janina, F. (2016), "Acidity of vapor plume from cooling tower mixed with flue gases emitted from coal-fired power plant", *Sci. Total Environ.*, **554**, 253-258.
- VGB-R610Ue (2005), "VGB-Guideline: structural design of cooling tower-technical guideline for the structural design, computation and execution of cooling towers", *Essen: BTR Bautechnik Bei Kühlturmen*.
- Viladkar, M.N., Karisiddappa, Bhargava, P. and Godbole, P.N. (2006), "Static soil-structure interaction response of hyperbolic cooling towers to symmetrical wind loads", *Eng. Struct.*, **28**(9), 1236-1251.
- Wang, H., Tao, T.Y. and Wu, T. (2016), "Wind power spectra for coastal area of East Jiangsu Province based on SHMS", *Wind Struct.*, **22**(2), 235-252.
- Witek, U. and Grote, K. (2015), "Substitute wind concept for elastic stability of cooling tower shells", *Mater. Member Behavior*, 500-513.
- Zhang, J.F., Chen, H., Ge, Y.J., Zhao, L. and Ke, S.T. (2014), "Effects of stiffening rings on the dynamic properties of hyperboloidal cooling towers", *Struct. Eng. Mech.*, **49**(5), 619-629.
- Zhao, L. and Ge, Y.J. (2010), "Wind Loading Characteristics of super-large cooling towers", *Wind Struct.*, **13**(4), 257-274.

